Supporting Information

Rapid Sintering of High-efficiency Phosphor-in-Glass Films for Laser-driven Light Source

Pengfei Wang, Hang Lin*, Guoxin Chen, Weitong Weng, Yue Xu, Yi Lin, Ju Xu, Yao Cheng, Yuansheng Wang*

Affiliations

State Key Laboratory of Structural Chemistry, Fujian Institute of Research on the Structure of Matter, Chinese Academy of Sciences, Fuzhou, Fujian, 350002, China

Pengfei Wang, Hang Lin, Yao Cheng

Fujian Science & Technology Innovation Laboratory for Optoelectronic Information of China, Fuzhou, Fujian, 350108, China

Hang Lin

Key Laboratory of Optoelectronic Materials Chemistry and Physics, Fujian Institute of Research on the Structure of Matter, Chinese Academy of Sciences, Fuzhou, Fujian, 350002, China

Pengfei Wang, Hang Lin, Yue Xu, Yi Lin, Ju Xu, Yao Cheng, Yuansheng Wang

University of Chinese Academy of Sciences, Beijing, 100049, China

Pengfei Wang, Yue Xu

Public Technology Center, Ningbo Institute of Materials Technology and Engineering, Chinese Academy of Sciences, Ningbo, Zhejiang, 315201, China

Guoxin Chen

South China University of Technology, Guangzhou, Guangdong, 510641, China

Weitong Weng

Corresponding author

Hang Lin, E-mail: lingh@fjirsm.ac.cn

Yuansheng Wang, E-mail: yswang@fjirsm.ac.cn

Table of Contents

Supplementary Fig. 9 PersL decay curves of $SrAl_2O_4$:Eu, Dy PiGF samples prepared using the RTA technique (monitored at 523 nm after 5 min of excitation at 365 nm); the insets in the upper half show digital photographs of the luminescent samples of the prepared samples in daylight and after stopping the UV light source irradiation; and the insets in the lower half show the potentials of the samples for the optical storage applications.

Supplementary Fig. 10 SEM image and the related particle size distribution statistics of glass powders.

Supplementary Fig. 11 Micro-CT 3D images of 10 s sintered glass film. The inset shows void size distribution of glass film sintered at 10 and the results of quantitative analysis of porosity. Observation volume: 1000 × 1000 × 86 μm^3.

Supplementary Fig. 12 X-ray diffraction pattern of the sintered glass film demonstrating an amorphous structure.

Supplementary Fig. 13 SEM images and particle size distribution statistics of SCASN:Eu phosphor.

Supplementary Fig. 14 Magnified SEM images of the surface of SCASN:Eu PiGF.

Supplementary Fig. 15 Sintering evolution of PiGF.

Supplementary Fig. 16 PL decay curves of SCASN:Eu phosphor powders, SCASN:Eu PiGF-RTA and SCASN:Eu PiGF-TS.

Supplementary Fig. 17 Thermal quenching properties of SCASN:Eu phosphor powders, SCASN:Eu PiGF-RTA and SCASN:Eu PiGF-TS.

Supplementary Fig. 18 a Digital photographs of phosphor wheels of SCASN:Eu PiGF with different thicknesses and PtoG. The **b** output luminous flux and **c** luminous efficiency of SCASN:Eu PiGFs (PtoG = 1:4, 2:3, 1:1, 3:2, 4:1) as a function of the incident laser power and incident laser power density. The **d** output luminous flux and **e** luminous efficiency of SCASN:Eu PiGFs (thickness = 50 μm, 69 μm, 86 μm , 99 μm, 107 μm, 130 μm) as a function of the incident laser power and incident laser power density.

Supplementary Fig. 19 EL spectra of SCASN:Eu PiGF-RTA (thickness = 50 μm, 69 μm, 86 μm , 99 μm, 107 μm, 130 μm, PtoG = 1:1) under laser excitation at different powers.

Supplementary Fig. 20 EL spectra of SCASN:Eu PiGF-RTA (PtoG = 1:4, 2:3, 1:1, 3:2, 4:1, 86 μm) under laser excitation at different powers.

Supplementary Fig. 21 EL spectra of SCASN:Eu-PiGF-TS.

Supplementary Fig. 22 PL and PLE spectra of $BaSi_2O_2N_2$:Eu PiGF-RTA, CASN:Eu PiGF-RTA, *β*-SiAlON:Eu PiGF-RTA, and *α*-SiAlON:Eu PiGF-RTA, and optical and fluorescence photographs at 365 nm excitation.

Supplementary Fig. 23 The luminous flux of **a** $BaSi_2O_2N_2$:Eu PiGF, **b** *β*-SiAlON:Eu PiGF, **c** CASN:Eu PiGF, and **d** *α*-SiAlON:Eu PiGF phosphor wheels sintered by RTA and TS method as a function of the incident laser power and incident laser power density.

Supplementary Fig. 24 EL spectra of $BaSi_2O_2N_2$:Eu phosphor wheels fabricated by the **a** RTA and **b** TS methods under laser excitation at different powers.

Supplementary Fig. 25 EL spectra of β-SiAlON:Eu phosphor wheels fabricated by the **a** RTA and **b** TS methods under laser excitation at different powers.

Supplementary Fig. 26 EL spectra of CASN:Eu phosphor wheels fabricated by the **a** RTA and **b** TS methods under laser excitation at different powers.

Supplementary Fig. 27 EL spectra of α-SiAlON:Eu phosphor wheels fabricated by the **a** RTA and **b** TS methods under laser excitation at different powers.

Supplementary Table 1 IQE/EQE and Abs of SCASN:Eu phosphor powders, SCASN:Eu PiGF-RTA and SCASN:Eu PiGF-TS.

Supplementary Table 2 Comparison of IQE/EQE of all inorganic red luminescent materials.

Supplementary Table 3 Luminous flux and luminescence efficiency of S-PiGF-RTA and S-PiGF-TS under excitation by increasing the incident blue laser power density from 1.27 W/mm^2 to 27.07 W/mm^2.

Supplementary Table 4 IQE of the fabricated nitride and oxynitride PiGFs via the RTA and TS methods and the original phosphor powders.

Supplementary Table 5 Comparison of luminous flux and luminous efficacy of all inorganic red luminescent materials.

Supplementary Fig. 1 Digital photographs of the (a) RTA device, and (b) quartz holder and silicon wafers inside the device.

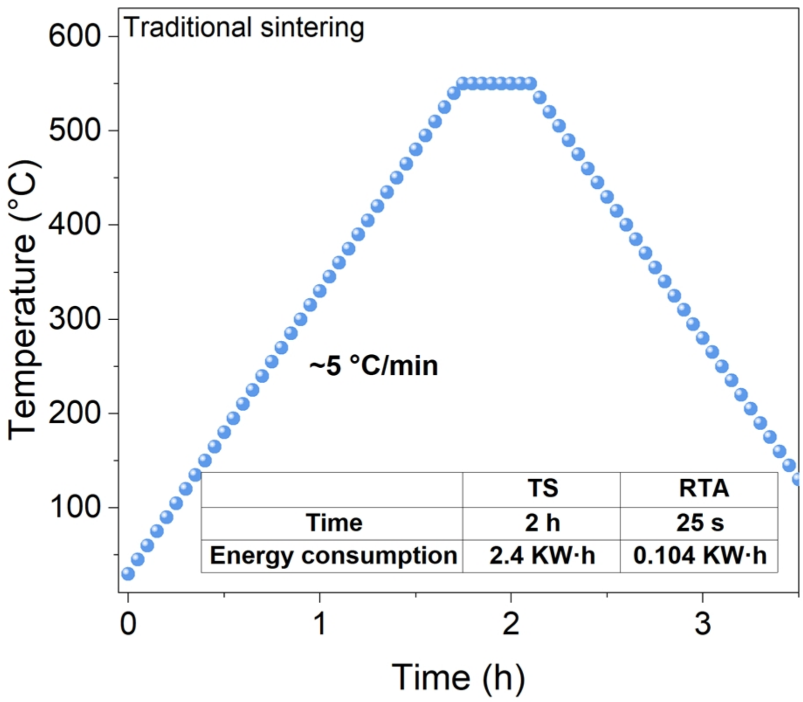

Supplementary Fig. 2 Heating curve of traditional sintering method in a muffle furnace.

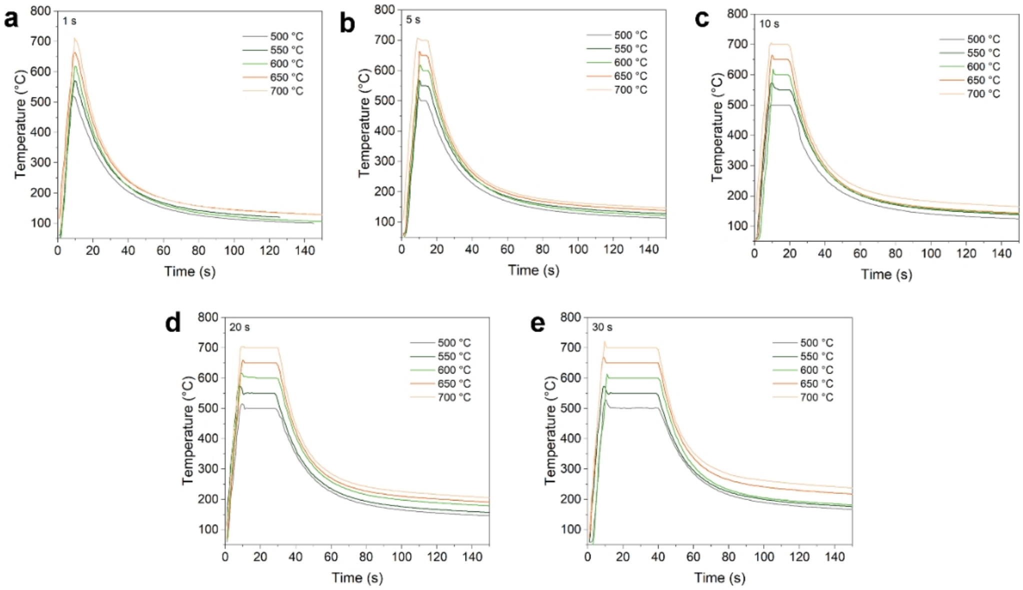

Supplementary Fig. 3 Heating curves of RTA process at 500°C, 550°C, 600°C, 650°C, 700°C for sintering 1s, 3s, 5s, 7s, 10s respectively.

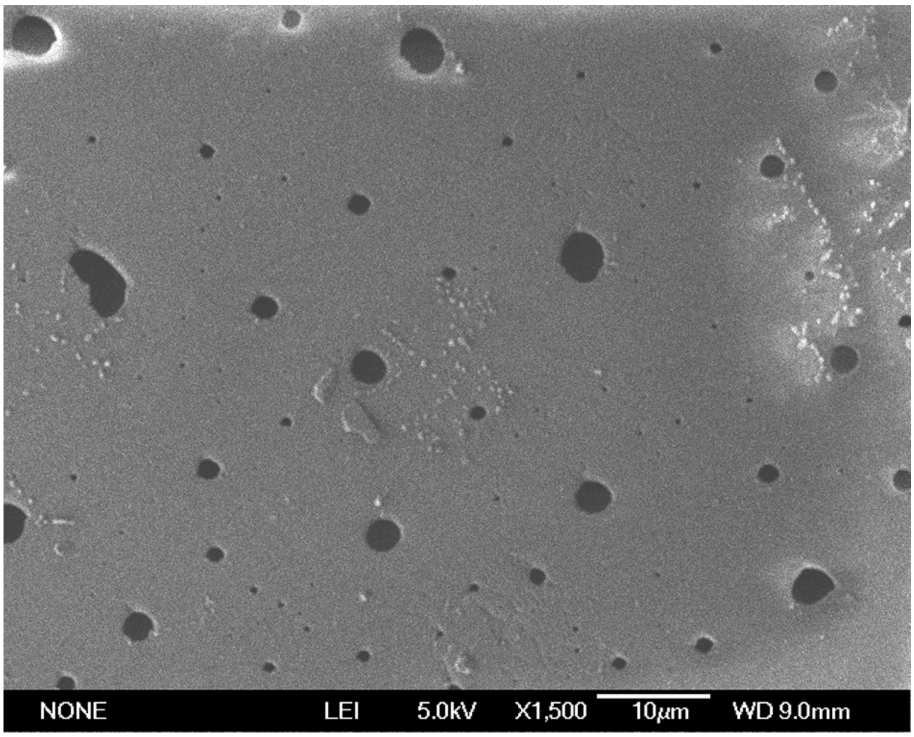

Supplementary Fig. 4 SEM image of the surface of the glass film sintering at 700 ℃ for 30 s.

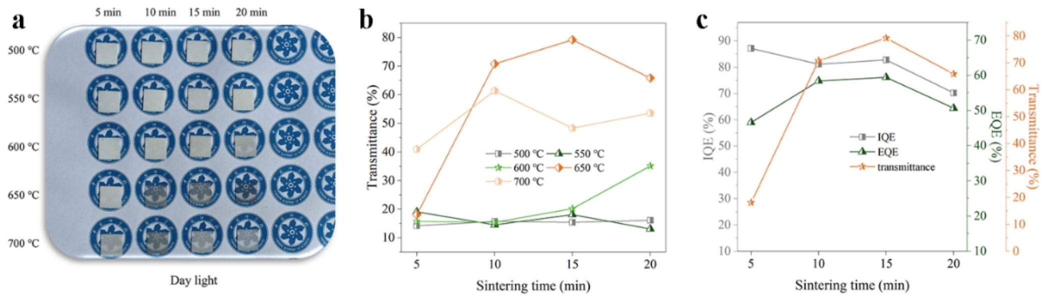

Supplementary Fig. 5 Process optimization of Traditional sintering methods.

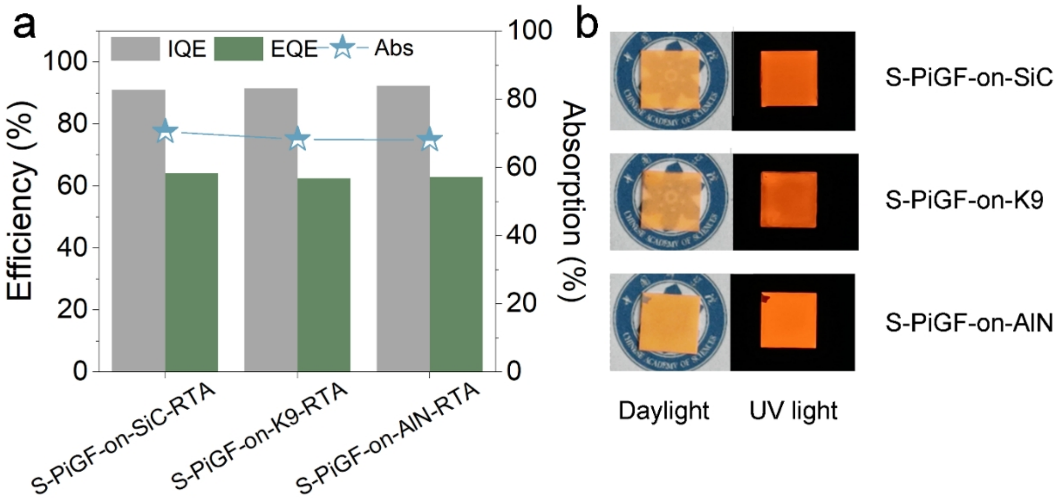

Supplementary Fig. 6 a IQE/EQE and absorption (Abs) of SCASN:Eu PiGF sintered on different substrates via RTA process. **b** Digital photographs of PiGF on different substrates under daylight and UV light.

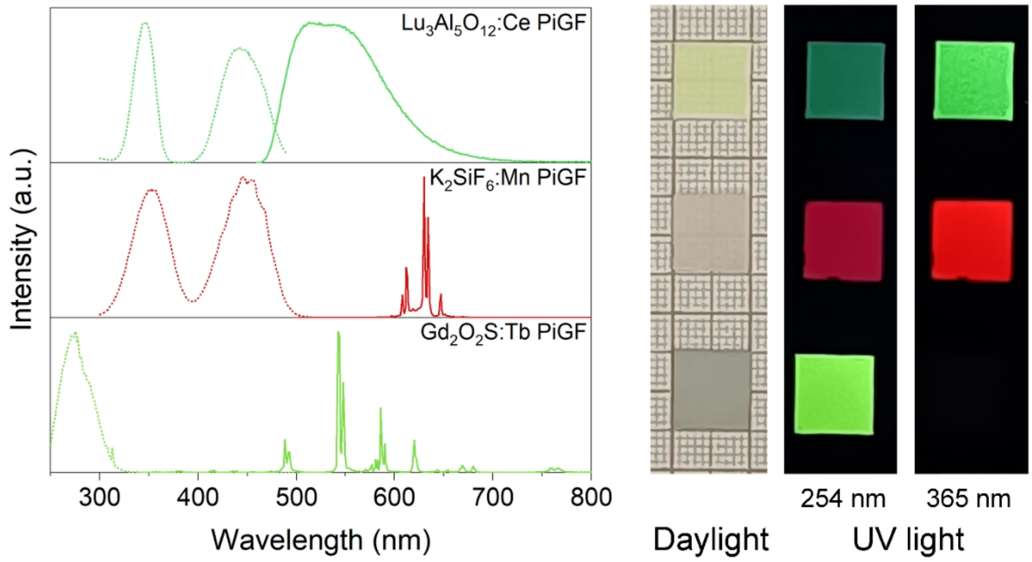

Supplementary Fig. 7 PL and PLE spectra of $Lu_3Al_5O_{12}$:Ce PiGF, K_2SiF_6:Mn PiGF and Gd_2O_2S:Tb PiGF, and optical and fluorescence photographs at 254 nm and 365 nm excitation.

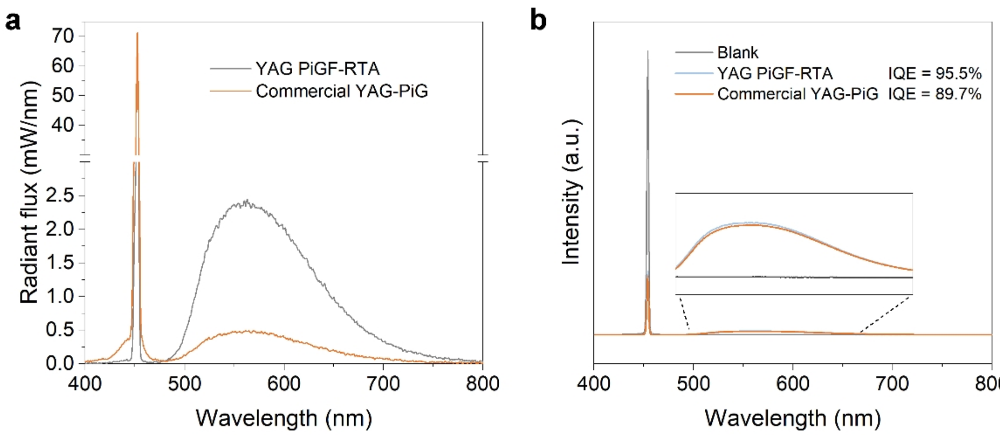

Supplementary Fig. 8 a EL spectra of YAG PiGF-RTA and commercial YAG-PiG under 1 W laser excitation. **b** Quantum efficiency of YAG PiGF-RTA and commercial YAG-PiG.

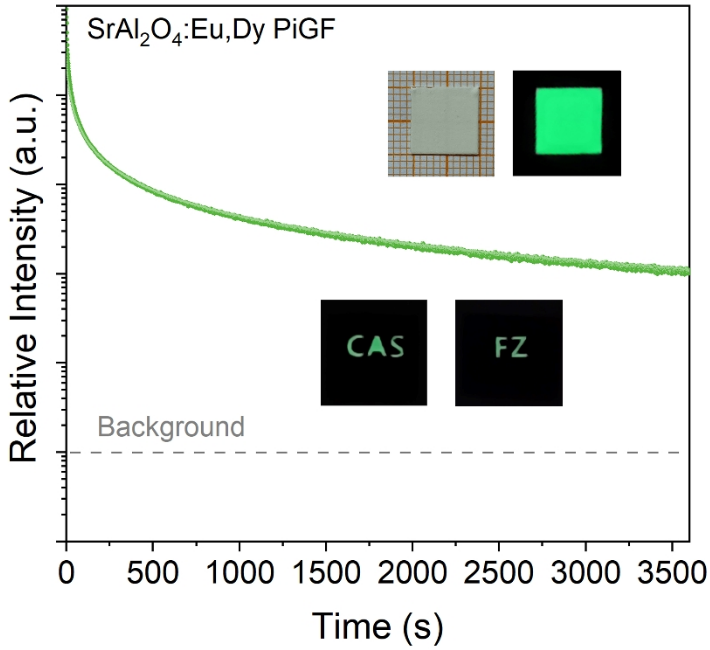

Supplementary Fig. 9 PersL decay curves of $SrAl_2O_4$:Eu, Dy PiGF samples prepared using the RTA technique (monitored at 523 nm after 5 min of excitation at 365 nm); the insets in the upper half show digital photographs of the luminescent samples of the prepared samples in daylight and after stopping the UV light source irradiation; and the insets in the lower half show the potentials of the samples for the optical storage applications.

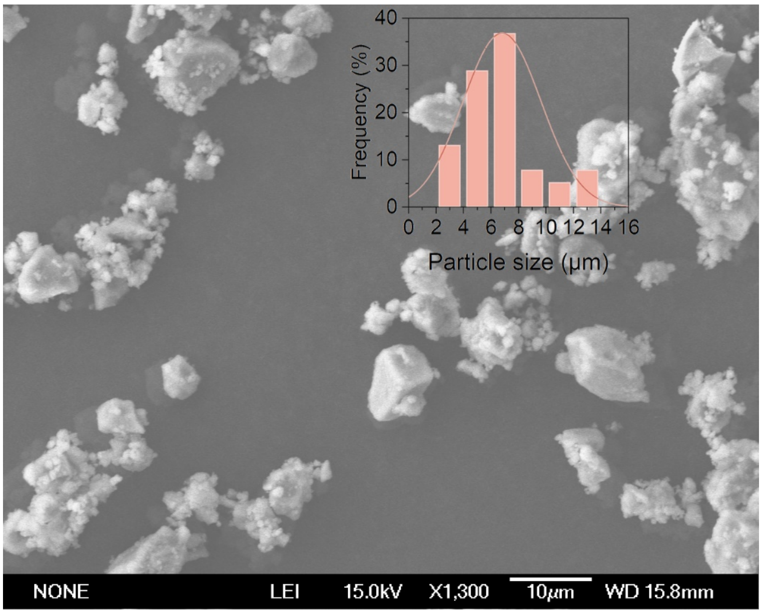

Supplementary Fig. 10 SEM image and the related particle size distribution statistics of glass powders.

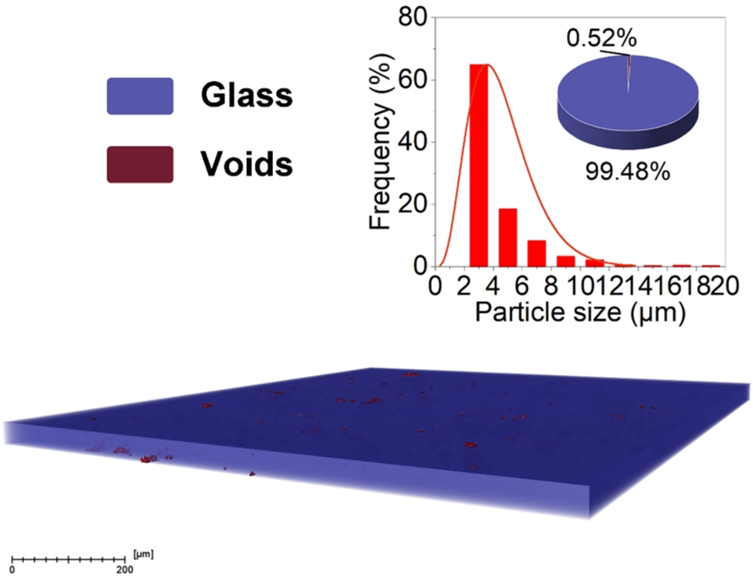

Supplementary Fig. 11 Micro-CT 3D images of 10 s sintered glass film. The inset shows void size distribution of glass film sintered at 10 and the results of quantitative analysis of porosity. Observation volume: 1000 × 1000 × 86 μm^3.

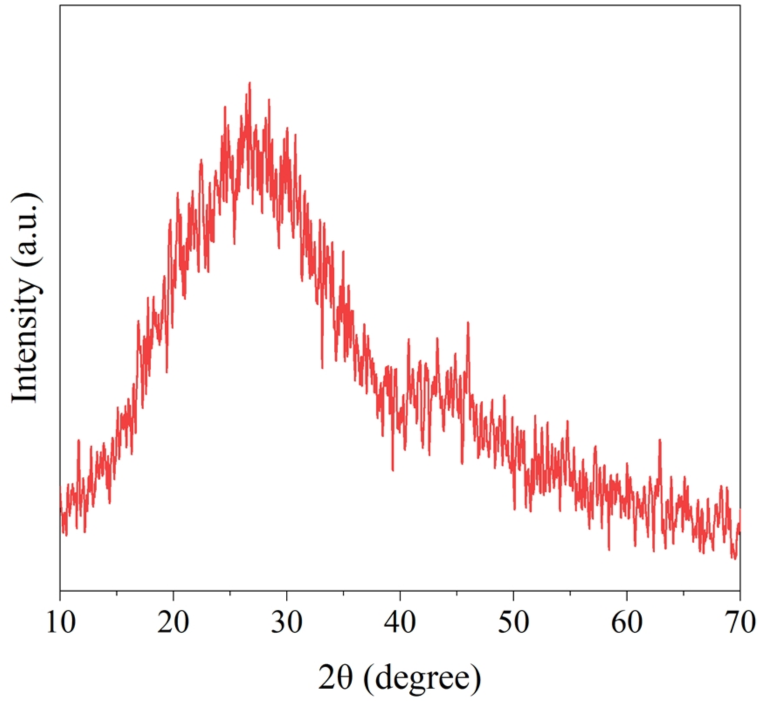

Supplementary Fig. 12 X-ray diffraction pattern of the sintered glass film demonstrating an amorphous structure.

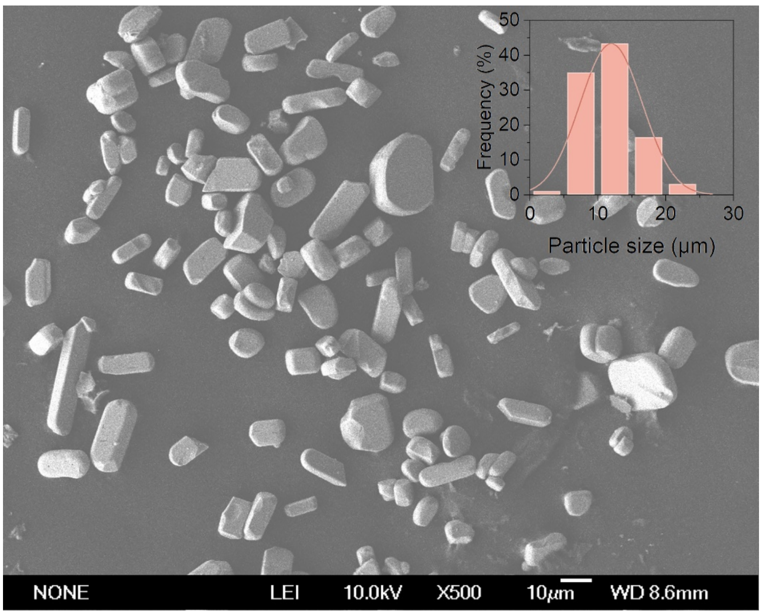

Supplementary Fig. 13 SEM images and particle size distribution statistics of SCASN:Eu phosphor.

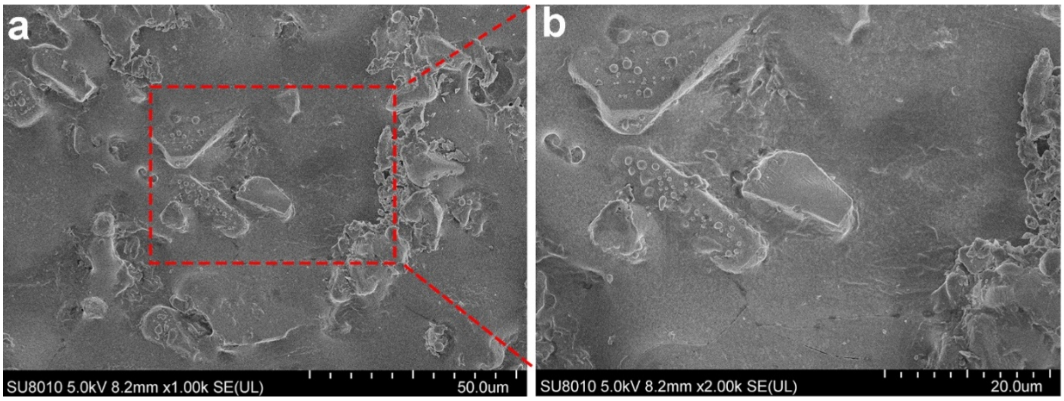

Supplementary Fig. 14 Magnified SEM images of the surface of SCASN:Eu PiGF.

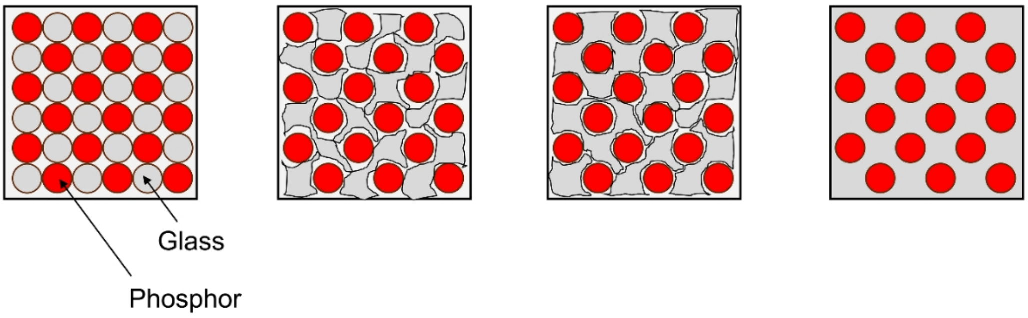

Supplementary Fig. 15 Sintering evolution of PiGF.

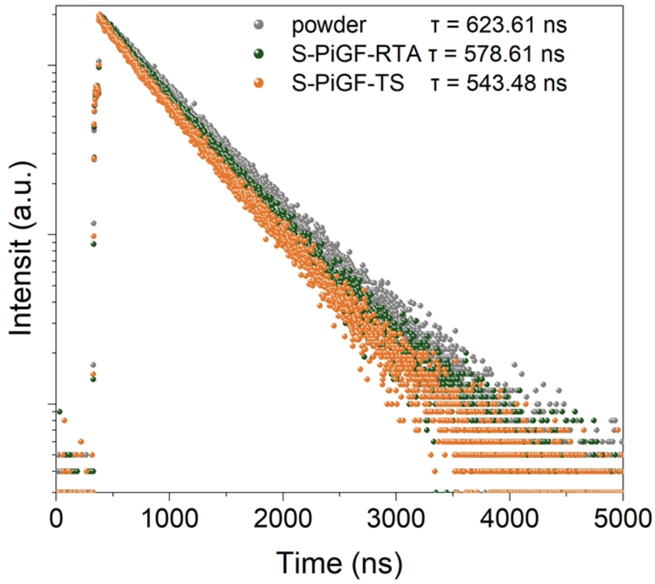

Supplementary Fig. 16 PL decay curves of SCASN:Eu phosphor powders, SCASN:Eu PiGF-RTA and SCASN:Eu PiGF-TS.

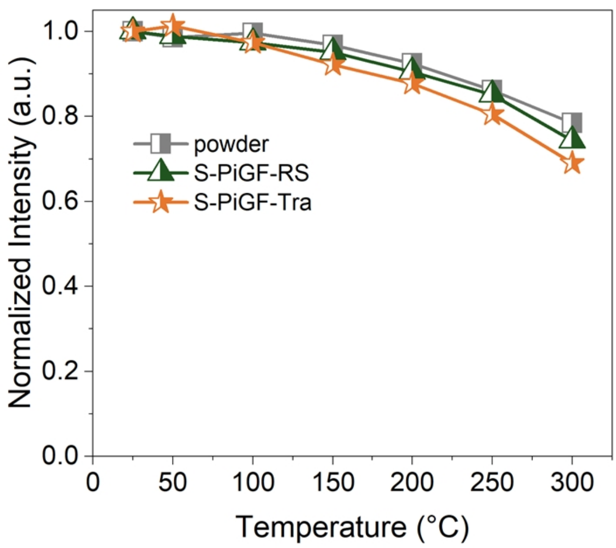

Supplementary Fig. 17 Thermal quenching properties of SCASN:Eu phosphor powders, SCASN:Eu PiGF-RTA and SCASN:Eu PiGF-TS.

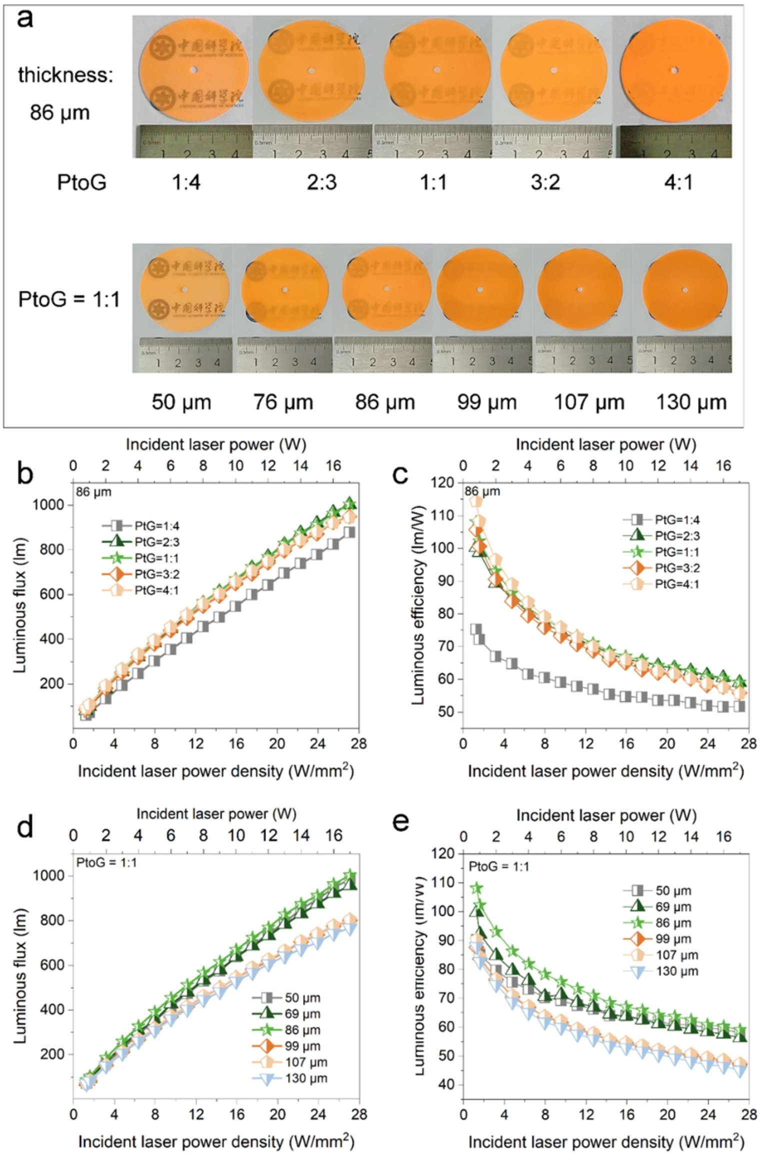

Supplementary Fig. 18 a Digital photographs of phosphor wheels of SCASN:Eu PiGF with different thicknesses and PtoG. The **b** output luminous flux and **c** luminous efficiency of SCASN:Eu PiGFs (PtoG = 1:4, 2:3, 1:1, 3:2, 4:1) as a function of the incident laser power and incident laser power density. The **d** output luminous flux and **e** luminous efficiency of SCASN:Eu PiGFs (thickness = 50 μm, 69 μm, 86 μm , 99 μm, 107 μm, 130 μm) as a function of the incident laser power and incident laser power density.

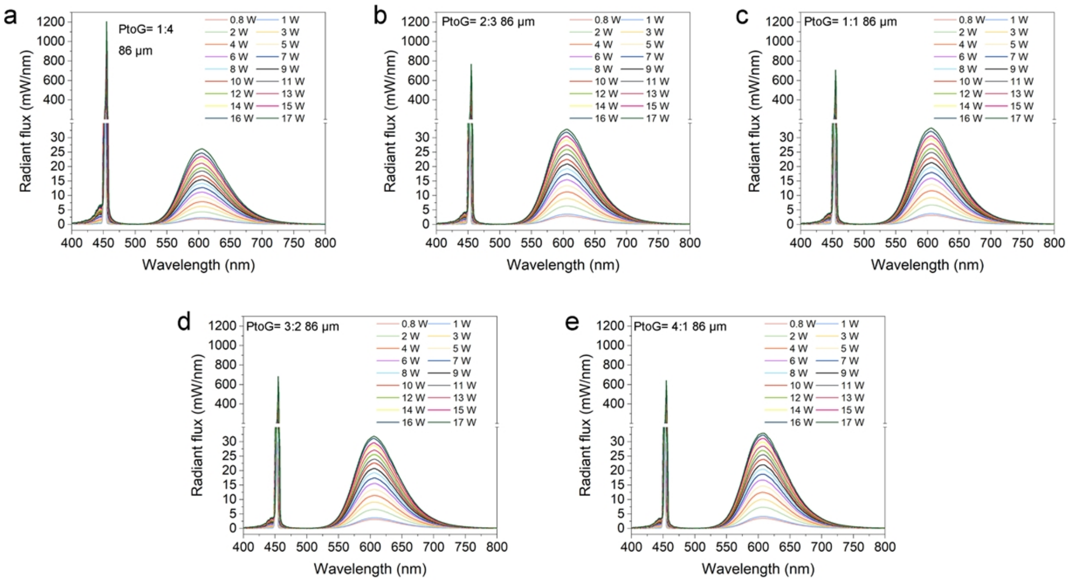

Supplementary Fig. 19 EL spectra of SCASN:Eu PiGF-RTA (thickness = 50 μm, 69 μm, 86 μm , 99 μm, 107 μm, 130 μm, PtoG = 1:1) under laser excitation at different powers.

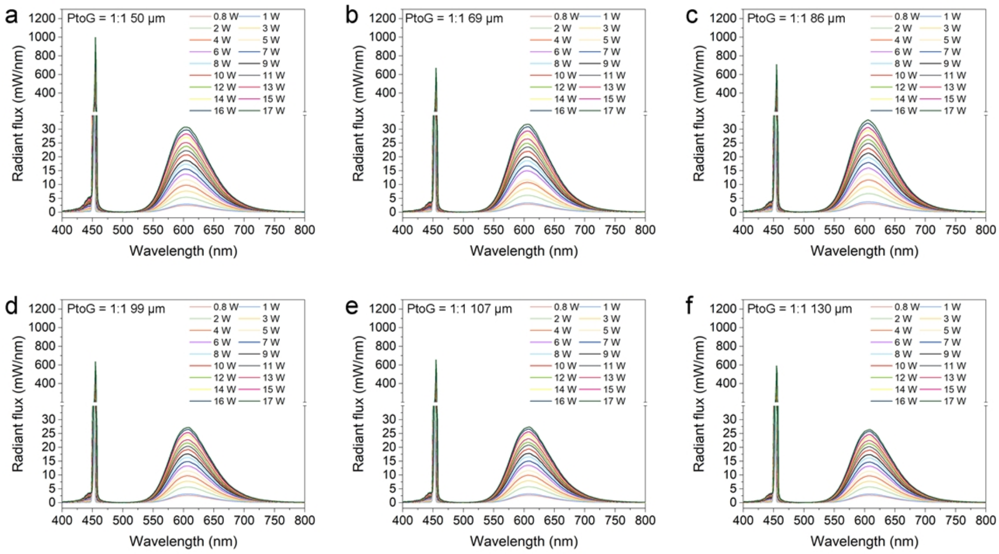

Supplementary Fig. 20 EL spectra of SCASN:Eu PiGF-RTA (PtoG = 1:4, 2:3, 1:1, 3:2, 4:1, 86 μm) under laser excitation at different powers.

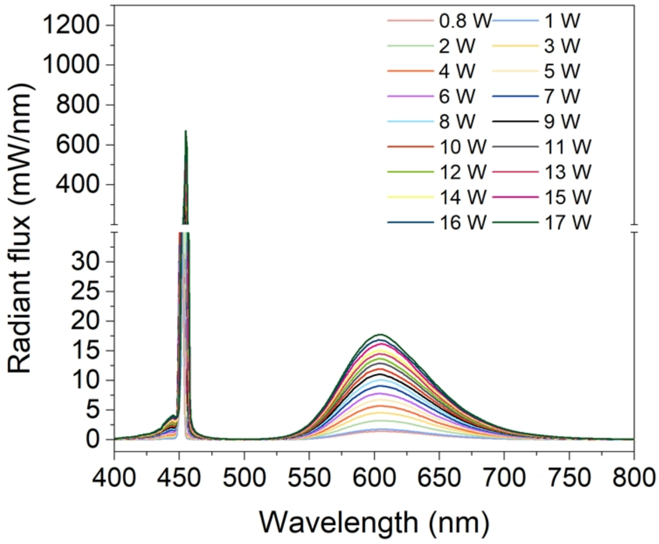

Supplementary Fig. 21 EL spectra of SCASN:Eu-PiGF-TS.

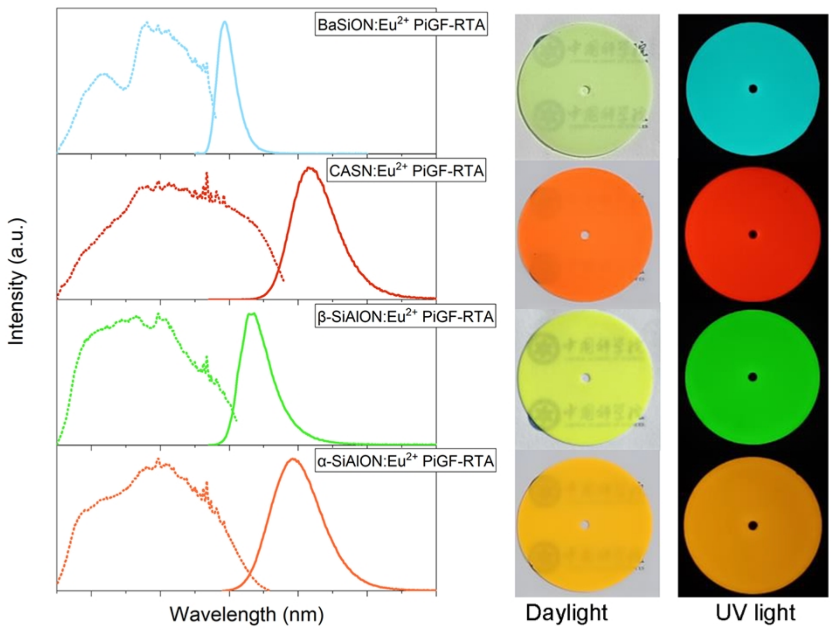

Supplementary Fig. 22 PL and PLE spectra of $BaSi_2O_2N_2$:Eu PiGF-RTA, CASN:Eu PiGF-RTA, *β*-SiAlON:Eu PiGF-RTA, and *α*-SiAlON:Eu PiGF-RTA, and optical and fluorescence photographs at 365 nm excitation.

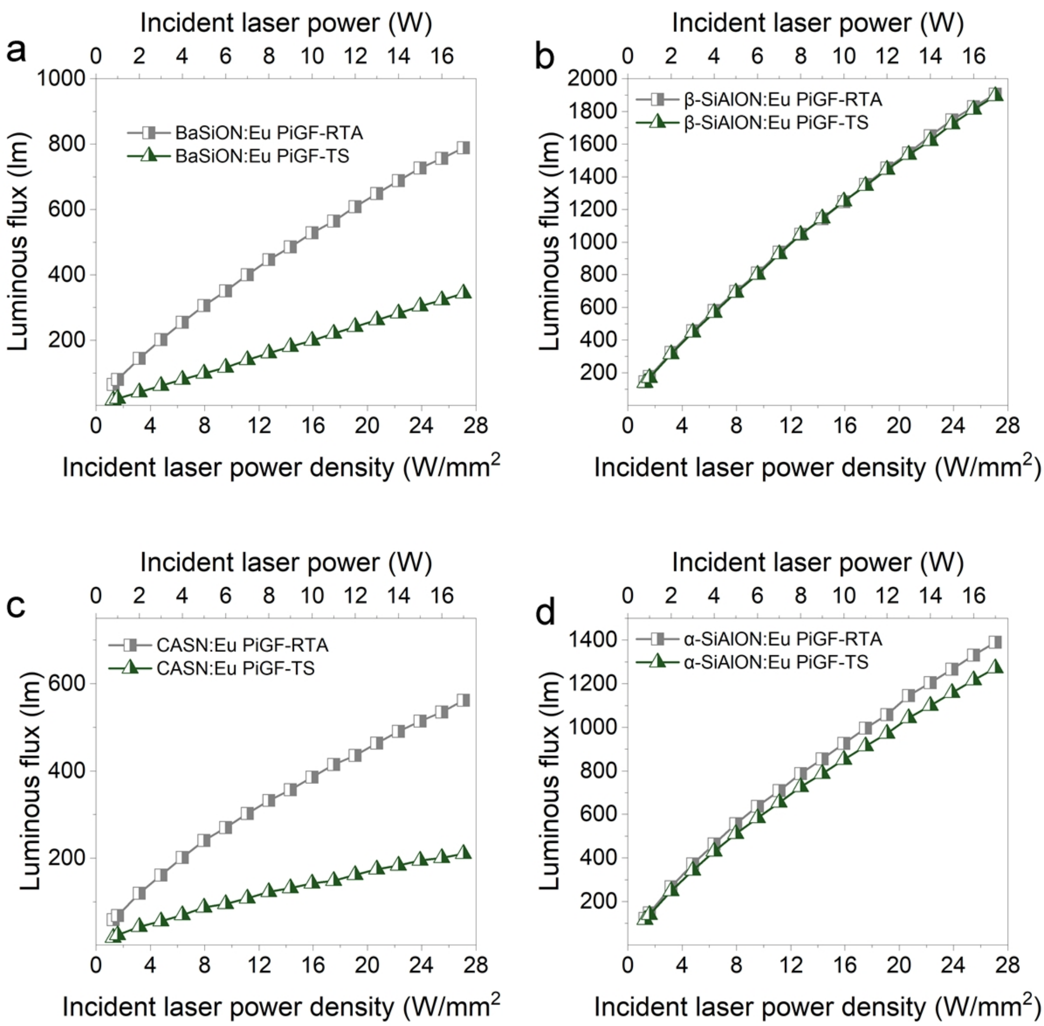

Supplementary Fig. 23 The luminous flux of **a** $BaSi_2O_2N_2$:Eu PiGF, **b** *β*-SiAlON:Eu PiGF, **c** CASN:Eu PiGF, and **d** *α*-SiAlON:Eu PiGF phosphor wheels sintered by RTA and TS method as a function of the incident laser power and incident laser power density.

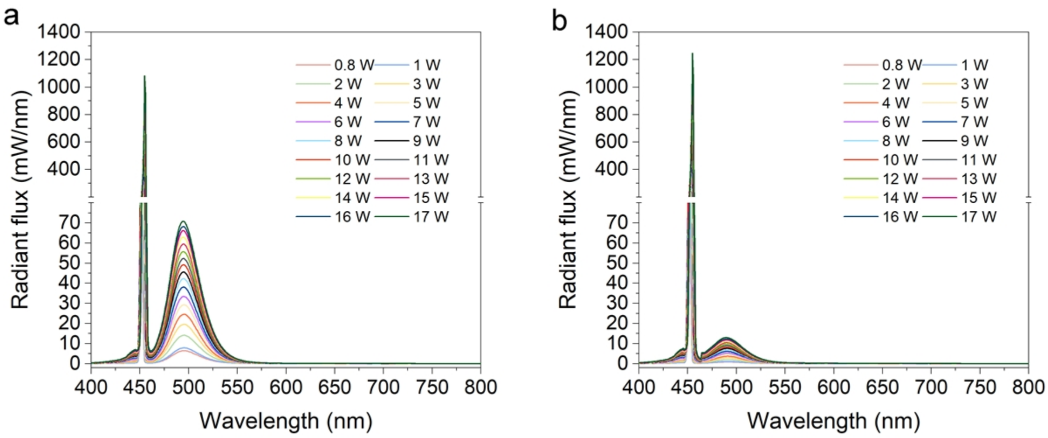

Supplementary Fig. 24 EL spectra of $BaSi_2O_2N_2$:Eu phosphor wheels fabricated by the **a** RTA and **b** TS methods under laser excitation at different powers.

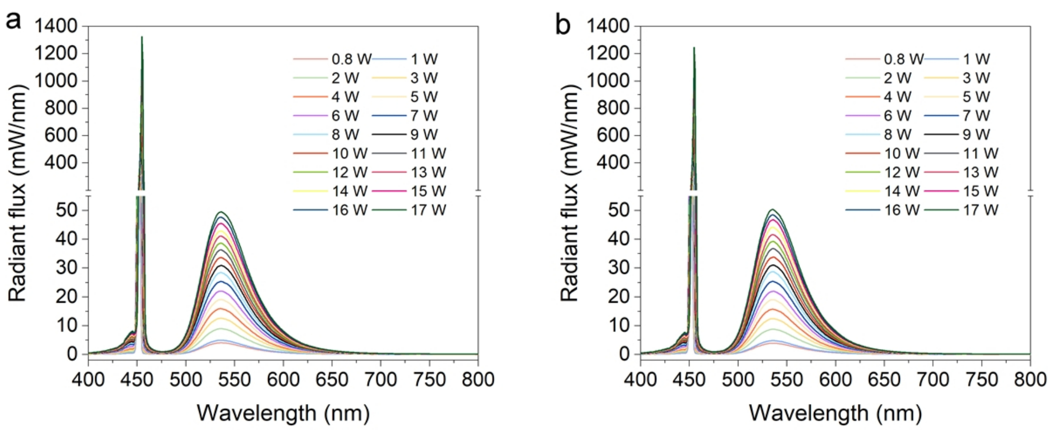

Supplementary Fig. 25 EL spectra of *β*-SiAlON:Eu phosphor wheels fabricated by the **a** RTA and **b** TS methods under laser excitation at different powers.

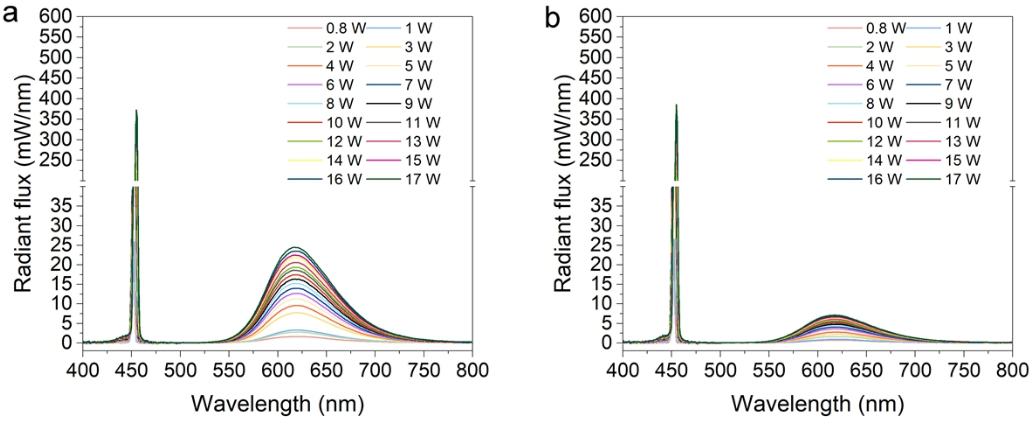

Supplementary Fig. 26 EL spectra of CASN:Eu phosphor wheels fabricated by the **a** RTA and **b** TS methods under laser excitation at different powers.

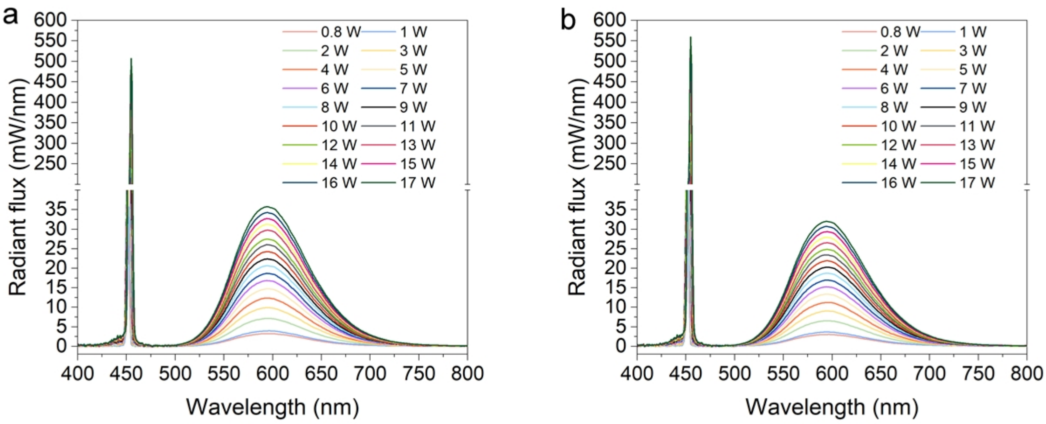

Supplementary Fig. 27 EL spectra of *α*-SiAlON:Eu phosphor wheels fabricated by the **a** RTA and **b** TS methods under laser excitation at different powers.

Supplementary Table 1 IQE/EQE and Abs of SCASN:Eu phosphor powders, SCASN:Eu PiGF-RTA and SCASN:Eu PiGF-TS.

Samples	**Excitation Wavelength (nm)**	**IQE**	**EQE**	**Abs**
SCASN:Eu powder	455 nm	96.5%	81.8%	84.0%
SCASN:Eu PiGF-RTA	455 nm	91.2%	65.9%	72.3%
SCASN:Eu PiGF-TS	455 nm	82.8%	59.4%	71.8%

Supplementary Table 2 Comparison of IQE/EQE of all inorganic red luminescent materials.

phosphor	Material	IQE	EQE	Ref.
$CaAlSiN_3:Eu^{2+}$	PiGF	79 %	-	[1]
$CaAlSiN_3:Eu^{2+}$	PiGF	83 %	-	[2]
$CaAlSiN_3:Eu^{2+}$	PiGF	70.7 %	63.8 %	[3]
$CaAlSiN_3:Eu^{2+}$	PiGF	71 %	-	[4]
$CaAlSiN_3:Eu^{2+}$	PiGF	89%	56 %	[5]
$CaAlSiN_3:Eu^{2+}$	PiGF	66.7 %	-	[6]
$CaAlSiN_3:Eu^{2+}$	PiGF	54.4%	40.8 %	[7]
$CaAlSiN_3:Eu^{2+}$	PiG	-	53 %	[8]
$CaAlSiN_3:Eu^{2+}$	Ceramic	28.5 %	17.4 %	[9]
$CaAlSiN_3:Eu^{2+}$	Ceramic	-	60 %	[10]
$SrAlSiN_3:Eu^{2+}$	PiG	75.6 %	-	[11]
Calson:Ce	PiGF	31.2 %	19.7 %	[12]
$Mg_2Al_4Si_5O_{18}:Eu^{2+}$	Ceramic	87.4 %	71.2 %	[13]
$(SrCa)AlSiN_3:Eu^{2+}$	**PiGF**	**91.2 %**	**65.9 %**	**This work**

Supplementary Table 3 Luminous flux and luminescence efficiency of S-PiGF-RTA and S-PiGF-TS under excitation by increasing the incident blue laser power density from 1.27 W/mm^2 to 27.07 W/mm^2.

Laser power density (W/mm^2)	Laser power (W)	S-PiGF-RTA		S-PiGF-TS	
		Luminous flux (lm)	Luminous efficacy (lm/W)	Luminous flux (lm)	Luminous efficacy (lm/W)
1.27	0.8	86.49	108.11	41.39	51.74
1.59	1	102.26	102.26	51.386	51.39
3.18	2	186.06	93.03	94.269	47.13
4.78	3	258.93	86.31	134.64	44.88
6.37	4	327.66	81.92	169.69	42.42
7.96	5	391.59	78.32	203.2	40.64
9.55	6	454.34	75.72	235.82	39.30
11.15	7	512.74	73.25	276.41	39.49
12.74	8	568.16	71.02	308.56	38.57
14.33	9	616.08	68.45	338.7	37.63
15.92	10	670.03	67.00	368.39	36.84
17.52	11	724.59	65.87	399.22	36.29
19.11	12	769.84	64.15	425.34	35.45
20.70	13	828.57	63.74	457.13	35.16
22.29	14	875.32	62.52	480.6	34.33
23.89	15	912.84	60.86	515.57	34.37
25.48	16	963.9	60.24	542.19	33.89
27.07	17	1004	59.06	569.67	33.51

Supplementary Table 4 IQE of the fabricated nitride and oxynitride PiGFs via the RTA and TS methods and the original phosphor powders.

Phosphor type	**Powder**	**RTA**	**TS**
$BaSi_2O_2N_2$:Eu	50.4%	44.2%	17.6%
CASN:Eu	92.3%	70.9%	59.8%
β-SiAlON:Eu	87.4%	72.4%	72.1%
α-SiAlON:Eu	89.3%	81.8%	76.7%

Supplementary Table 5. Comparison of luminous flux and luminous efficacy of all inorganic red luminescent materials.

phosphor	Material	Test mode	Luminous flux (lm)	Luminous efficacy (lm/W)	Ref.
$CaAlSiN_3:Eu^{2+}$	PiGF	static/transmission	25	21	[1]
$CaAlSiN_3:Eu^{2+}$	PiGF	static/reflection	1576	-	[2]
$CaAlSiN_3:Eu^{2+}$	PiGF	static/transmission	164	-	[14]
$CaAlSiN_3:Eu^{2+}$	PiG	static/transmission	43	46	[8]
$CaAlSiN_3:Eu^{2+}$	Ceramic	static/reflection	-	11	[10]
$CaAlSiN_3:Eu^{2+}$	Ceramic	static/reflection	51	-	[15]
$Mg_2Al_4Si_5O_{18}:Eu^{2+}$	Ceramic	static/reflection	523	24	[13]
$Sr_{0.8}Ca_{0.2}AlSiN_3:Eu^{2+}$	**PiGF**	rotation/reflection	2379	140	**This work**

References

1. Xu J., *et al.* Design of a $CaAlSiN_3$:Eu/glass composite film: Facile synthesis, high saturation-threshold and application in high-power laser lighting. *J Eur Ceram Soc* **40**, 4704-4708 (2020).

2. Xu J., *et al.* $CaAlSiN_3$:Eu/glass composite film in reflective configuration: A thermally robust and efficient red-emitting color converter with high saturation threshold for high-power high color rendering laser lighting. *Ceram Int* **47**, 15307-15312 (2021).

3. Liu Z. H., *et al.* $CaAlSiN_3:Eu^{2+}/Lu_3Al_5O_{12}:Ce^{3+}$ phosphor-in-glass film with high luminous efficiency and CRI for laser diode lighting. *J Mater Chem C* **9**, 3522-3530 (2021).

4. Huang Q. G., *et al.* Toward high-quality laser-driven lightings: chromaticity-tunable phosphor-in-glass film with "phosphor pattern" design. *Laser Photonics Rev* **16**, 2200040 (2022).

5. Li S. X., Huang L. H., Guo Y. Q., Wang L. & Xie R. J. A super-high brightness and excellent colour quality laser-driven white light source enables miniaturized endoscopy. *Materials Horizons* **10**, 4581-4588 (2023).

6. Huang Q. G., *et al.* Patterned glass ceramic design for high-brightness high-color-quality laser-driven lightings. *J Adv Ceram* **11**, 862–873 (2022).

7. Ding W. T., *et al.* Dual-emitting phosphor-glass composites by the melt-quenching method for high-quality laser lighting. *Ceram Int* **48**, 34602-34609 (2022).

8. Zhang Y. J., *et al.* A high quantum efficiency $CaAlSiN_3:Eu^{2+}$ phosphor-in-glass with excellent optical performance for white light-emitting diodes and blue laser diodes. *Chem Eng J* **401**, 125983 (2020).

9. Peng X. L., *et al.* Highly thermal conductive red-emitting AlN-$CaAlSiN_3:Eu^{2+}$ composite phosphor ceramics for high-power laser-driven lighting. *J Eur Ceram Soc* **41**, 5650-5657 (2021).

10. Li S. X., Zhu Q. Q., Wang L., Tang D. M. & Xie R. J. $CaAlSiN_3:Eu^{2+}$ translucent ceramic: a promising robust and efficient red color converter for solid state laser displays and lighting. *J Mater Chem C* **4**, 8197-8205 (2016).

11. Bao H. R., *et al.* $SrAlSiN_3:Eu^{2+}$ containing phosphor-in-glass: A color converter for solid state laser lighting. *Opt Mater* **126**, 112169 (2022).

12. Wang L., Wei R., Zheng P., You S. H. & Xie R. J. Realizing high-brightness and ultra-wide-color-gamut laser-driven backlighting by using laminated phosphor-in-glass (PiG) films. *J Mater Chem C* **8**, 1746-1754 (2020).

13. Chen W. B., *et al.* Red-emitting cordierite ceramic enabling general healthy warm white laser lighting. *Laser Photonics Rev* **18**, 2300963 (2024).

14. Liang Y. Y., Bao S. Y., Wang Y., Liang X. J., Wang X. & Xiang W. D. Highly thermally stable red phosphor-in-glass films for high-power laser lighting. *J Lumin* **248**, 118930 (2022).

15. Peng X. L., *et al.* Microstructure tailoring of red-emitting AlN-$CaAlSiN_3:Eu^{2+}$ composite phosphor ceramics with higher optical properties for laser lighting. *J Eur Ceram Soc* **42**, 3339-3344 (2022).